

Simulating the effect of the Sgr A* accretion flow on the appearance of G2 after pericenter

David Abarca^{1*}, Aleksander Sądowski^{1*}, Lorenzo Sironi^{1,2*}

¹ *Harvard-Smithsonian Center for Astrophysics, 60 Garden St., Cambridge, MA 02134, USA*

² *NASA Einstein Fellow*

30 October 2018

ABSTRACT

We study the dynamical interaction of the G2 cloud with the accretion flow around Sgr A* by means of three-dimensional, hydrodynamic simulations. We show the effects of the rotating accretion flow on the evolution of G2 by projecting the cloud density onto the plane of the sky, and extracting position-velocity diagrams. We study a number of possible orientations of the cloud orbit with respect to the disk. We find that once the center of mass of the cloud has crossed the pericenter, the differences between models becomes significant. Models with the cloud counter-rotating with respect to the disk are expected to reach higher blue-shifted line of sight velocities. The spatial extent of the emission depends strongly on the cloud-to-disk inclination angle. Future imaging and spectroscopy of G2 emission will shed light both on the structure of the Sgr A* disk and on the properties of the cloud.

Key words: accretion, accretion discs – black hole physics – methods: numerical

1 INTRODUCTION

Gillessen et al. (2012) discovered a gaseous object (the G2 cloud) approaching the supermassive black hole (SMBH) in the center of the Galaxy on a very eccentric orbit. It is expected to approach as close as $R = 4800 R_G$ ($R_G = GM_{\text{BH}}/c^2 = 6.3 \cdot 10^{11}$ cm is the black hole gravitational radius, where M_{BH} is the black hole mass) from Sgr A* in early 2014 (Gillessen et al. 2013b), and its mass has been estimated to be roughly $3M_{\oplus}$ (Gillessen et al. 2012). The nature of the cloud is still debated. A pressure supported gas cloud or a momentum supported wind from a star (where the external pressure is balanced by its ram pressure) may explain equally well the observed size, shape, and range of line of sight velocities (Schartmann et al. 2012). Although, the fact that the cloud is followed by an additional structure ('tail') of comparable mass and very similar orbit, Gillessen et al. (2012); Burkert et al. (2012) support the scenario of a gas cloud which was formed not so long ago in the Galactic center.

On its way, the cloud evolves under the tidal gravitational field of the SMBH. The resulting stretching has been clearly observed in combined astrometric and spectroscopic data. The pressure supported gas cloud model predicts that the object will be tidally disrupted after crossing the pericenter, while the stellar wind model predicts that the object survives the passage. However, the tidal forces are not the only ones acting on the cloud. Sgr A* is known to accrete gas with a relatively low accretion rate of $10^{-9} - 10^{-7} M_{\odot}/\text{yr}$ (see next Section). However, even such a small rate implies an ac-

cretion flow with densities and velocities in its inner region comparable to those of G2. Therefore, the cloud itself is likely to be affected by its dynamical interaction with the accretion disk of Sgr A*. The outcome will depend on the properties of the cloud and the accretion flow and orientation of the cloud orbit with respect to the accretion disk axis. The point of this paper is to study how this interaction affects the observables around and after pericenter assuming that G2 is a pressure supported gas cloud.

The G2 cloud has so far been observed by two groups with adaptive optics astrometry and spectroscopy based on the Keck and VLT telescopes (Gillessen et al. 2012, 2013a,b; Phifer et al. 2013). They were able to extract not only images of the cloud approaching the Galactic center but also the position along the orbit (arclength along the center of mass trajectory to the pericenter) vs line of sight velocity diagrams, which allowed for very precise determination of the orbital parameters of the cloud center of mass. As the cloud becomes tidally elongated, the observed emission no longer follows a single Keplerian orbit (Gillessen et al. 2013b). The spatial distribution and line of sight properties of the emission are likely to be affected by dynamical interactions with the accretion flow and to trace the properties of Sgr A*'s rotating atmosphere. The interaction will likely also affect the plane of sky view of the cloud. Therefore, it is not unreasonable to think that the observations of the cloud near and after the epoch of pericenter will shed some light on the so far poorly constrained properties of the Sgr A* accretion disk and/or the G2 cloud.

These hopes are especially justified in the view of the soon to come leading infrared imaging project, GRAVITY. It is a second generation VLTI, four beam combiner with 4 milliarcsecond (mas) imaging resolution for a $m_K \sim 15$ source (Kendrew et al. 2012;

* E-mail: dabarca@cfa.harvard.edu (DA); asadowski@cfa.harvard.edu (AS); lsironi@cfa.harvard.edu (LS)

Gillessen et al. 2010). First astronomical light for this instrument is planned for 2014, possibly early enough to witness the tail end of G2 pericenter passage and to contribute to the imaging of G2 after it has crossed the pericenter.

1.1 Previous work

Much work has already been done on simulating G2's interaction with Sgr A*. Schartmann et al. (2012) used two-dimensional, high resolution, hydrodynamic simulations to evolve two different origin scenarios: a compact cloud scenario with a uniform density structure formed shortly before first observations, and a spherical shell with an apocenter among the disks of young stars in the Galactic Center. They modeled the atmosphere of Sgr A* by neglecting rotation and choosing the temperature to maintain hydrostatic equilibrium.

Anninos et al. (2012) performed three-dimensional, moving-mesh, hydrodynamic simulations. They assumed a spherical cloud in pressure equilibrium as in Schartmann et al. (2012). They used two different models for the SMBH atmosphere, one following Schartmann et al. (2012) which is convectively unstable, and a more physically motivated one from Yuan et al. (2003) with a density and temperature profile based on observations, again without rotation. They adopted an initial temperature of 10^4 K and claimed that the radiative cooling timescale is short enough to maintain this temperature. They support the conclusions of Schartmann et al. (2012) and Burkert et al. (2012) that the cloud must have been formed shortly before its first observation. They did not expect the cloud to survive its pericenter passage.

Saitoh et al. (2012) attempted to address the radiative cooling problem using N-body/smoothed particle hydrodynamics. Using the same background setup as Schartmann et al. (2012) but scaling the disk density as a parameter, they predicted a maximum bolometric luminosity of $\sim 100L_{\odot}$ which should be visible in the near IR. They did not account for rotation.

Sądowski et al. (2013) studied the formation of the bow-shock in front of the cloud when penetrating the Sgr A* accretion disk. They used a turbulent and magnetized background model of the disk based on a general relativistic magneto-hydrodynamic (GRMHD) simulation. The cloud had to be scaled down to fit within the computational domain. Its density, velocity and mass were also scaled to produce a consistently scaled model of the entire system. The interaction was resolved under full GRMHD, yet with very limited resolution in azimuth.

The simulations we report in this work do not neglect the rotation of the Sgr A* atmosphere and, for the first time, allow for the study of the impact of the orientation of the cloud orbit with respect to the axis of rotation of the atmosphere. As with most of the previous authors, we neglect the magnetic field. On one hand, resolving the magneto-rotational instability (MRI) without scaling down the cloud is impossible with current computational resources, on the other magnetic fields are not likely to substantially change the nature of the interaction, since they are subdominant with respect to gas pressure.

The main alternative to the cloud scenario, the compact source scenario, is addressed by Ballone et al. (2013) who simulated various setups of G2 as an outflow from a central source using two-dimensional simulations in cylindrical coordinates. Assuming a zero angular momentum orbit, they tracked the cloud from apocenter until very near Sgr A*. They found that their simulations were consistent with the observed extent of G2 on the position-velocity diagrams.

Guillochon et al. (2014) studied the origin of G2 as the result of a tidal disruption event of a star orbiting the Galactic center. Using 3D, hydrodynamic code FLASH, Guillochon et al. (2014) found that the returning gas tidally stripped from a star may fragment and explain the clumpy nature of G2 and its observed tail.

2 Sgr A* DISK

The SMBH at the center of our Galaxy is known to accrete gas at fairly low level of $\dot{M}_{\text{BH}} = 10^{-9} - 10^{-7} M_{\odot}/\text{yr}$ (Yuan et al. 2003; Marrone et al. 2007; Mościbrodzka et al. 2009; Dexter et al. 2010; Shcherbakov et al. 2012; Dibi et al. 2012). The accretion flow is radiatively inefficient and its properties are not yet well determined. The only well-established parameter besides the accretion rate at the BH is the density at the Bondi radius R_{B} , $n_{\text{B}} = 120 \text{ cm}^{-3}$, where $R_{\text{B}} = 2 \times 10^5 R_{\text{G}}$ (Baganoff et al. 2003). Recent Chandra observations of the region inside the Bondi radius suggest the density slope, $n \propto r^{-0.5}$ (Wang et al. 2013), but are far from being conclusive. To fill the gap between the BH and R_{B} one has to rely on numerical models of radiatively inefficient accretion flows (RIAFs).

Simulating accretion across such a wide range of scales (from the BH horizon to the Bondi radius) is a daunting challenge. Single simulations which resolve the BH horizon in general relativity are limited by their computational cost to two decades in radius (e.g., Narayan et al. 2012b). Larger scales may be resolved but only by means of coupling separate simulations together (Yuan et al. 2012).

There is a consensus, based on a limited number of long duration simulations performed so far, that RIAFs are characterized by significant mass loss leading to a shallower slope of the density distribution than the slope, $n \propto r^{-3/2}$, predicted by the standard ADAF model (Narayan & Yi 1994). The slope favored by simulations is close to $n \propto r^{-1}$ and for Sgr A* it qualitatively agrees with the measured value of the accretion rate at the horizon.

In this work we use the Sgr A* accretion flow model put forward by Sądowski et al. (2013b). It is based on a long-duration GRMHD simulation of a RIAF (Narayan et al. 2012b) which has converged up to $R \lesssim 200R_{\text{G}}$. The power-law profiles of density (normalized to fit the density at the Bondi radius), temperature, and azimuthal velocity were extrapolated along the slopes implied by the data inside the resolved domain. Such a solution provides axisymmetric accretion flow structure as a function of radius and polar coordinate in the whole region between the BH and the Bondi radius, which reasonably reproduces the Sgr A* accretion flow under the assumption that its structure is self-similar there.

While we consider several scenarios for the orientation of the G2 orbit relative to the accretion flow around Sgr A*, recent millimeter VLBI observations of the Event Horizon Telescope collaboration (Broderick et al. 2011) suggest that G2 is roughly co-rotating with respect to the spin direction of Sgr A*. There are large uncertainties on these estimates however. We will consider the co-rotating scenario as our fiducial model.

3 CLOUD MODEL

The G2 cloud has been observed in infrared since 2004. The combined spectroscopic and imaging data have allowed for a precise determination of the orbital parameters of the cloud center of mass (Gillessen et al. 2012, 2013a,b; Phifer et al. 2013). The position and line of sight velocity measurements have been successfully reproduced by a model consisting of test particles initiated at year

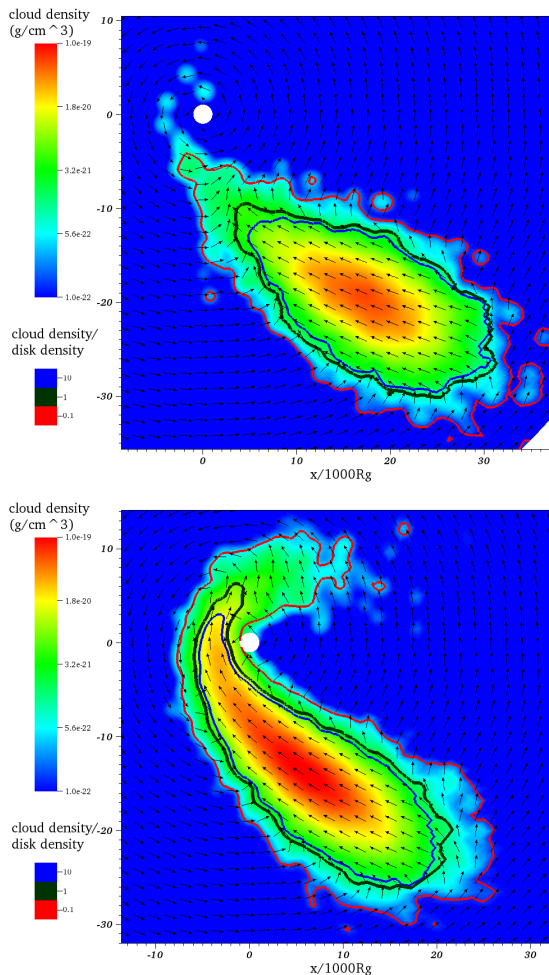


Figure 1. Density of the cloud in its orbital plane at 2012.4 (top) and 2013.4 (bottom panel). The cloud was based on the test particle model as given in Gillessen et al. (2013b) and superimposed on top of counter-rotating Sgr A* disk. Contours show the ratio of cloud to disk densities. The black contour encircles the region dominated by the cloud density.

$t = 2000.0$ as a Gaussian spherical cloud with full width at half maximum (FWHM) of 42 milliarcseconds (mas) with velocity dispersion $\sigma = 120$ km/s (Gillessen et al. 2013b). Although this approach qualitatively reproduces the observed position and velocity distribution, it has a few flaws that we address below.

The test particle approach only accounts for gravitational forces, neglecting the dynamical interaction of the cloud with the atmosphere. To test if this assumption is satisfied, we took the cloud model as given in Gillessen et al. (2013b) and propagated the cloud of test particles until 2012.4 and 2013.4, i.e., roughly until the epochs for which position-velocity diagrams were plotted in Gillessen et al. (2013a) and Gillessen et al. (2013b), respectively. We then superimposed the implied cloud density and momentum field on top of the background disk model. Figure 1 shows with colors the cloud density distribution and contours of cloud to disk density ratio. The black contour, in particular, surrounds the region where the cloud density dominates. Qualitatively speaking, whatever is outside is likely to be significantly affected by the interaction with the disk.

The position-velocity diagrams shown in Figure 2 quantify this effect for $t = 2013.4$. The top panel shows the line of sight velocities and positions along the orbit for the test particle cloud model as proposed by Gillessen et al. (2013b) and corresponds to the observed distributions at this epoch. The middle and bottom panels show the cloud gas velocities after superimposing the cloud on the counter- and co-rotating disk atmosphere respectively. The velocities were calculated by taking a density weighted average between the disk and test particle cloud velocities at a given location. The cloud gas outside the black contour is indeed dominated by the disk and no longer moves with the original velocity. As a result the position-velocity diagram changes. Most striking is that there are hardly any blue-shifted (negative line of sight velocities) particles, both for co- and counter-rotating disks, which were directly detected in IR at that time by Gillessen et al. (2013b) implying that the cloud constructed following their model cannot reproduce the observed distributions after taking the interaction with the disk into account. Since we want to study the cloud properties at even later epochs we need to construct a cloud model that after consistent inclusion of dynamical interactions would reasonably reproduce the features observed so far.

Another feature of the Gillessen et al. (2013b) cloud model which may seem unrealistic is the high velocity dispersion ($\sigma = 120$ km/s) assumed at $t = 2000.0$. The cloud is producing line emission implying very a low temperature (10^4 K) inconsistent with the adopted value of σ . To avoid this and still reproduce the observed properties of the cloud (size and range of line of sight velocities) one could consider a cloud of test particles with zero velocity dispersion initiated at $t = 2000.0$ as a spherical, constant density cloud of size significantly larger than the corresponding characteristic length of the Gillessen et al. (2013b) model (similar to model F3 in Sądowski et al. 2013). The increased size would balance the lack of velocity dispersion and produce comparable range of line of sight velocities. Such a flat density cloud would have much heavier outer layers which would not be so easily affected by the disk gas. It would also be close to isothermal what is a reasonable physical configuration for a gaseous object like the G2 cloud.

Following this approach we have constructed a cloud model which reasonably satisfies the constraints coming from observations up to $t = 2013.4$ (presented and discussed in Section 5.3). We adopted a flat density cloud of test particles at $t = 2000.0$ with zero velocity dispersion and radius $R_0 = 100$ mas. Each particle was assumed to have the cloud center of mass velocity at that time. Test particles were propagated until $t_{\text{init}} = 2012.0$ along Keplerian orbits. At that time the cloud was smoothed using a Gaussian kernel with characteristic width $w_{\text{kernel}} = 1000 R_G$, scaled up to match the desired cloud mass, and superimposed on top of the disk by summing up disk and cloud momenta and densities. The pressure was kept at the disk-implied value resulting in a cloud colder than the disk by 2-3 orders of magnitude, maintaining pressure equilibrium. We consider pressure equilibrium to be the most natural initial condition for our simulations

Figure 3 shows the total density (top) and temperature (bottom panel) as result from the superposition of the cloud on to the disk atmosphere at $t_{\text{init}} = 2012.0$ for the fiducial model M1. Such a setup was then used as the initial condition for the full hydrodynamical simulation, which includes the dynamical interaction of the cloud with the accretion flow.

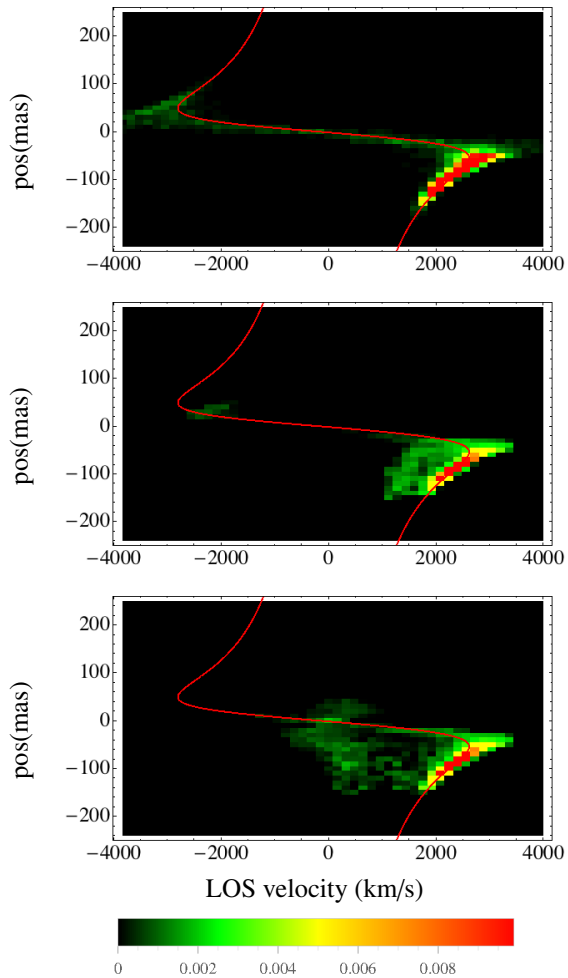


Figure 2. Position along the orbit - velocity diagrams at 2013.4 for the cloud based on the Gillessen et al. (2013b) test particle model. The top panel corresponds to test particles unaffected by the disk. The middle and bottom panels show the position and velocities after superimposing the cloud model on top of counter- and co-rotating disks, respectively. Colors show the fractional mass of the cloud.

4 NUMERICAL SETUP

We simulate the interaction of G2 cloud with the Sgr A* accretion disk using the hydrodynamic part of general relativistic, radiation, hydrodynamic code KORAL (Sądowski et al. 2013a). Due to the size of the cloud orbit and the related computational cost we were not able to resolve the BH horizon. The inner boundary was set to $R_{\text{in}} = 700R_G$ for most of the models¹. The background atmosphere was set according to the disk model of Sądowski et al. (2013b). On the top of it we superimposed the cloud, as described in Section 3, at the time $t_{\text{init}} = 2012.0$ and evolved the resulting system until and beyond the epoch of cloud pericenter $t_0 = 2014.25$.

The grid used in most of the simulations consisted of 160 uniformly spaced points in the full range of azimuthal angle ϕ , 80 quasi-logarithmically spaced points in radius between R_{in} and $R_{\text{out}} = 50000 R_G$, and 81 cells in the polar angle θ uniformly covering the range $\theta_0 < \theta < \pi - \theta_0$, with $\theta_0 = 0.05$. We adopted outflow

¹ This fact makes the general relativistic part of KORAL redundant.

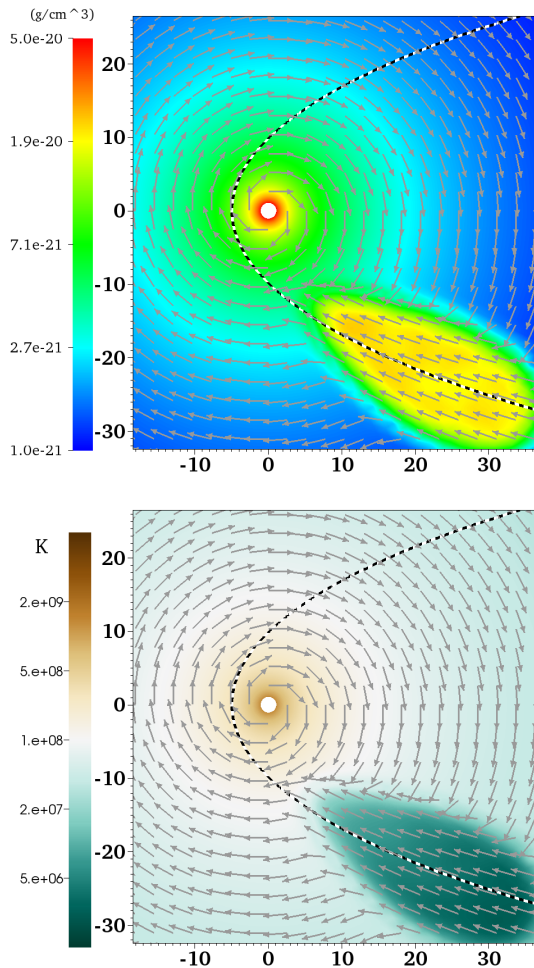


Figure 3. The initial conditions for the density (top) and temperature (bottom) at the cloud orbit for the fiducial model M1. Vectors show the velocity field and the dashed line shows the cloud center of mass orbit.

boundary conditions (BC) at the inner and outer edges, periodic BC in the azimuth and transmissive BC in the polar angle.

For all the models, the cloud orbit coincides with the equatorial plane of the grid so that one could expect the cloud to propagate in that plane and avoid the polar axis (where a cone with opening angle $\pm\theta_0$ has been cut off from the domain) as much as possible. To simulate arbitrary orientation of the cloud with respect to the disk we rotate the background disk atmosphere by the appropriate angle.

The model of the Sgr A* accretion flow given by Sądowski et al. (2013b) is supposed to qualitatively reproduce the structure of the real 3D accretion flow driven by magnetorotational instability. For obvious reasons it does not catch all the features of the turbulent MHD flow. It does not correspond to a hydrodynamical equilibrium torus (e.g., Abramowicz et al. 1978), either. As a result, when evolved under pure hydrodynamics, the atmosphere is neither in hydrostatic equilibrium nor convectively stable. To make the cloud interact with gas as similarly as possible to the assumed disk model, we follow the approach adopted by Schartmann et al. (2012) and evolve an extra passive tracer field which helps distinguishing the cloud-affected region from the parts of the rotating

atmosphere that have not yet interacted with the cloud. The tracer field is initiated at $t = t_{\text{init}}$ by setting its value to the fraction of density coming from the cloud,

$$\text{tr} = \frac{\rho_{\text{cl}}}{\rho_{\text{cl}} + \rho_{\text{disk}}}, \quad (1)$$

and ranges from 0 (far from the cloud) to 1 (inside the cloud). Then, it is passively evolved along the velocity field of the gas. At each time step we consider cells with $\text{tr} < 10^{-4}$ as unaffected by the cloud and smoothly reset the gas properties there to the original disk-model based values.

5 RESULTS

In this work, we report on eight different cloud and disk setups. The parameters are described in Table 1. We place the cloud in the plane of the disk both co-rotating (M1) and counter-rotating (M2) with the disk. We incline the cloud with respect to the disk at 60° (M3) which produces a co-rotating model and 120° (M4) which produces a counter-rotating model. We then take these two cases and reflect them across the cloud orbit (M5, M6). This does not change the dynamics of the cloud-disk interactions, but it does change the projection of the cloud onto the plane of the sky. We then adopt two more co-rotating clouds in the plane of disk with different cloud masses, one at $1 M_\oplus$ (M7, to assess the effect of a lower mass) and one at $300 M_\oplus$ (M8, to study ballistic-like cloud propagation).

Another parameter that defines the orientation of G2 orbit is the argument of periapsis (ω) which rotates the entire orbit around its angular momentum vector. When the orbit is in the plane of the disk, this has no effect on the dynamics of the system, but when the disk is inclined, ω determines when the cloud crosses the disk equatorial plane (Sądowski et al. 2013b). $\omega = \pi/2$ corresponds to pericenter lying in the equatorial plane of the disk. $\omega = 0$ implies that the cloud crosses the disk equatorial plane twice (at $t = t_0 \pm 0.45\text{yr}$) and the pericenter is off that plane. The impact of ω on the properties of the cloud gas after it has crossed the pericenter is secondary (the cloud plows through gas of similar properties but at different moments of time) and we decide to fix $\omega = 0$.

We have tested the effects of the numerical parameters we used in our simulations. Shown in Table 1, we ran a simulation at a higher resolution (P1), a simulation with a higher minimum radius (P2), a simulation with a grid that extends further in the polar direction (P3), and two simulations that use higher (10^{-3} , P4), and lower (10^{-5} , P5) critical tracer values. In all cases we observe no significant differences between our test runs and the fiducial model M1.

We also ran one simulation to test the effect of lowering the initial temperature of our cloud (P6). The observed temperature has been reported to be approximately 10^4K (Gillessen et al. 2012), but due to the pressure equilibrium we assume, our cloud is at a temperature of about 10^6K . We tested the effect of lowering the initial pressure, which was initially in equilibrium with the disk, by one order of magnitude which caused an equal decrease in temperature, and we found no significant difference in the evolution of the cloud.

5.1 Evolution of the cloud

In Fig. 4 we show the evolution of the gas density in the orbital plane of the cloud for our fiducial model (M1). Three different epochs are presented: 2013.4 (which corresponds to the observations in Gillessen et al. (2013b)), 2014.25 (the epoch of pericenter),

and 2014.6 (early August 2014). Overplotted on all of the images are arrows indicating the velocity unit vector. In this simulation, the cloud is co-rotating in the plane of the accretion disk, as can be seen from the velocity vectors. As the cloud approaches pericenter it is compressed by about two orders of magnitude before expanding again into the disk. The compression results mostly from tidal forces from the SMBH. After the cloud passes pericenter, the head of the cloud is significantly affected by the disk velocity and pulled away from the center of mass (CM) trajectory.

In Fig. 5, we have shown density in the orbital plane of the cloud at $t = 2014.6$ for six different runs. Upper left is the co-rotating run from Fig. 4. Upper middle is the same except for a counter-rotating cloud. In this case, the bulk of the cloud passes closer to the SMBH, indicating a loss of angular momentum which we measure to be approximately 30% of the initial value by adding shells of mass at decreasing contours of density to produce a cloud of a consistent mass between the final and initial states of the cloud and between different models. We then measured the magnitude of the difference of angular momentum between the initial and final states. At this distance, both disk pressure and tidal forces are greater, and so we observe more compression. The lower left and lower middle plots correspond to cloud orbits inclined at $i = 120^\circ$ (co-rotating) and $i = 60^\circ$ (counter-rotating), respectively. The plots are shown in the orbital plane, and so we can see underdense regions at the pericenter. They result from the disk pulling the cloud out of its orbit. It pulls it below the orbital plane before the pericenter, and towards the opposite direction after the pericenter. This effect is more clear in the 3D plots discussed in the next paragraph. We see the same pattern of tidal and pressure compression with these two runs, except to a lesser extent. The right most images are both of co-rotating clouds in plane of the disk, but for different cloud masses. Above we used a $300 M_\oplus$ cloud so that the cloud would be virtually unaffected by the disk, even near the SMBH. Below we used a $1 M_\oplus$ cloud to achieve the opposite effect of emphasizing the cloud interaction with the disk. Note that for the $300 M_\oplus$ cloud the density scale of the color scheme has been scaled with the cloud mass.

Shown in Fig. 6 are 3D contours of density at pericenter projected along the line of pericenter. The orbital plane is indicated by the blue stripe and the cloud moves horizontally to the left. The arrow indicates the rotation of the background accretion flow (the arrow head is always protruding from the plot). The top two images are of the cloud in the plane of the disk. We can see the cloud being disrupted but it is symmetrical with respect to the plane of the orbit. The counter-rotating cloud shows a much stronger interaction with the disk; the head is more strongly compressed in the direction of motion. The next two figures are for inclined orbits with respect to the disk. In this instance, we clearly observe the disk sweeping material out of the plane of the orbit. The next two images are the same as the previous two, but reflected across the plane of the orbit. We expect this effect to be observable. The last two images are of the $1 M_\oplus$ and $300 M_\oplus$ for which we scaled the contours in a similar way to Fig. 5. The $1 M_\oplus$ cloud is mostly lost in the disk. The $300 M_\oplus$ cloud is largely unaffected by the disk, but highly compressed in the plane of the orbit around the pericenter.

5.2 Sky plane images

In the interest of observables, we have projected the cloud onto the plane of the sky. We have assumed an optically thin cloud with luminosity strictly proportional to total gas density, including the disk density which we expect to be dominated by the cloud. We

Run	Disk Rotation	Inclination	Reflected	Mass (M_{\oplus})	$N(R)$	$N(\phi)$	$N(\theta)$	$R_{\text{in}}(R_G)$	$\theta_{\text{min}}(\text{rad})$	T_{crit}	P_{cl}
M1	co	0°	no	3	80	160	81	700	0.05	10^{-4}	P_{disk}
M2	counter	180°	no	3	"	"	"	700	"	"	"
M3	co	60°	no	3	"	"	"	1000	"	"	"
M4	counter	120°	no	3	"	"	"	"	"	"	"
M5	co	60°	yes	3	"	"	"	"	"	"	"
M6	counter	120°	yes	3	"	"	"	"	"	"	"
M7	co	0°	no	1	"	"	"	"	"	"	"
M8	co	0°	no	300	"	"	"	"	"	"	"
P1	co	0°	no	3	100	200	101	1000	0.05	10^{-4}	"
P2	"	"	"	"	80	160	81	1000	0.05	10^{-4}	"
P3	"	"	"	"	80	160	81	1000	0.03	10^{-4}	"
P4	"	"	"	"	80	160	81	1000	0.03	10^{-3}	"
P5	"	"	"	"	80	160	81	1000	0.03	10^{-5}	"
P6	co	0°	no	3	80	160	81	1000	0.05	10^{-4}	$P_{\text{disk}}/10$

Table 1. The parameters of the numerical models. $N(R)$, $N(\phi)$, $N(\theta)$ give the resolutions in R , ϕ , and θ respectively. R_{in} and θ_{min} are the minimal radial and polar coordinates. T_{crit} is the critical tracer field value. P_{cl} is the initial pressure of the cloud (all but P6 are in pressure equilibrium with the disk).

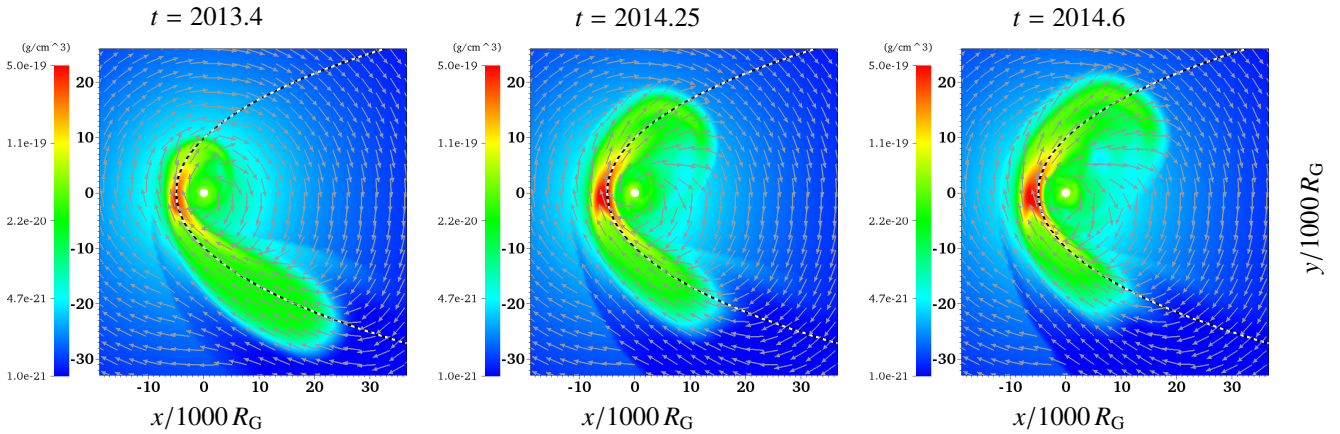


Figure 4. Cloud density plots for the co-rotating disk (model M1) corresponding to epochs $t = 2013.4, 2014.25, 2014.6$. The axes are in units of $1000 R_G$. The dashed line shows the center of mass orbit.

have rotated the cloud to the orbit orientation described in Gillessen et al. (2013b). We selected all the cells with a cutoff density of 10^{-21} g/cm^3 . We binned these cells from the simulation into a uniform grid on the sky and integrated ρ^2 along the line of sight, as this is directly proportional to flux for Case B recombination (Osterbrock & Ferland 2006). We plotted the fractional brightness on the sky, shown in Fig. 7. We then overplotted the center of mass orbit as projected onto the plane of the sky (green line).

A possible caveat to consider is the effect of the temperature of the cloud on its observability. Guillochon et al. (2014) have shown that the cooling rate decreases with temperature, which implies a decrease in brightness after pericenter.

We observe a clear difference between the counter- and co-rotating cases. The former is inside its orbit on the sky while the latter follows its orbit. The counter-rotating case is also denser near pericenter, which matches our observations in Fig. 5. For the inclined cases, we observed in Fig. 6 that material was pulled out of the plane of the cloud orbit. We can see this effect in Fig. 7 where the cloud material extends about 40 mas lower on the sky. The two inclined clouds follow the same pattern where the counter-rotating one is farther inside the orbit than the co-rotating one. The two images in the third row have been reflected across the plane of their orbits. This changes their shape on the sky significantly. Both of them appear to be in their orbits, but as we can see from Fig. 6, the bulk of the post pericenter cloud has been pushed out of the orig-

inal orbit aligned with the observer's line of sight. The final two images of Fig. 7 are the $1 M_{\oplus}$ and $300 M_{\oplus}$ clouds. The small cloud is affected and slowed down more by the disk and results in slightly more confined cloud projection. The big cloud effectively does not feel the disk and its front propagates faster.

Gillessen et al. (2012, 2013a,b), using the SINFONI spectrograph, have been able to spatially resolve the line of sight velocity of G2. In this paragraph we show the plane of sky velocity distributions for the simulations we performed without projecting the location on the cloud orbit (as was done by these authors and what we do in the next Section). For this purpose we took all the cells that lie above a certain density threshold, and binned them onto the sky in the same manner as for Fig. 7. We then computed a mass weighted average of line of sight velocity of all the cells that lie within a particular bin and plotted them on the sky. The plots correspond to the same cloud and disk setups as in Figs 6 and 7. Zero velocity is the same color as the background. Deep blue color corresponds to the largest velocities towards the observer. The velocities are the largest for counter-rotating clouds which pass closer to the SMBH. The inclined and reflected runs show higher velocities than the original inclined models because the velocity vectors of these clouds tend to lie more along the line of sight.

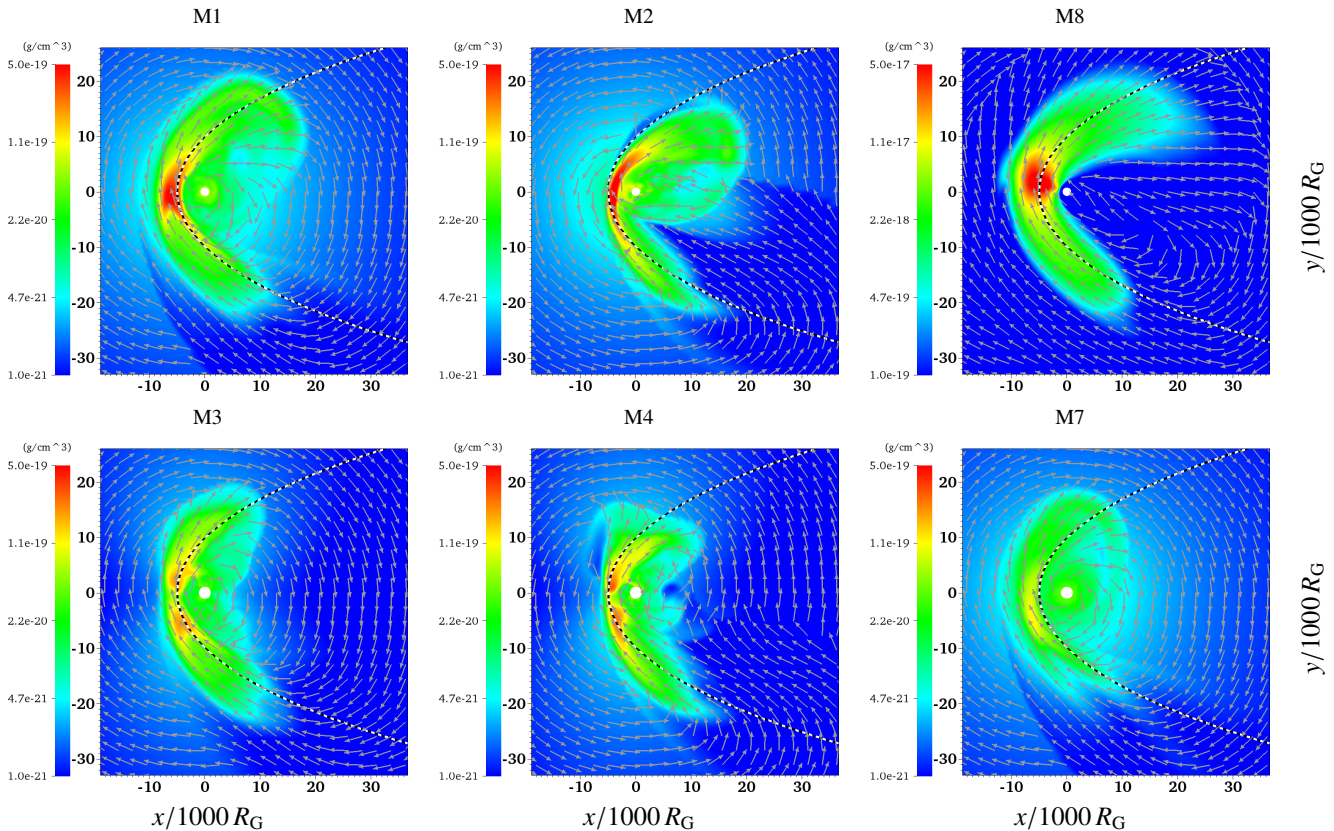


Figure 5. Cloud density in the plane of orbit at $t = 2014.6$. M5 and M6 are identical to M3 and M4. The axes are in units of $1000 R_G$. The arrows show the normalized velocity vector.

5.3 Position - velocity diagrams

The two observables of most interest for this physical system are the position along the orbit and the line of sight velocity. Plotting them together shows the tidal effects of the SMBH on the cloud shape and on the velocity dispersion (Gillessen et al. 2012, 2013a,b). We claim that the hydrodynamical effects of the disk are also apparent in these diagrams as deviations from the center of mass trajectories. We use our simulation data to plot these diagrams such that they are directly comparable with that in Gillessen et al. (2013b).

We compute the position - velocity diagrams by taking the cells above the same density threshold as before and binning them by their positions along the center of mass orbit, and their line of sight velocities. We extract the position along the orbit by projecting each cell location on the sky onto the nearest point on the projected center of mass trajectory. For each bin, we integrate ρ^2 . We then plot the fractional flux for each bin to indicate the distribution of light from the cloud.

In Fig. 9 we have produced position - velocity diagrams for the co-rotating cloud in the plane of the disk (model M1) at three epochs, 2013.4 to match the observations of Gillessen et al. (2013b), 2014.25 (pericenter), and 2014.6. At 2013.4, we have successfully produced some blue-shifted emission in qualitative agreement with observations. We see that as the cloud evolves, it loses angular momentum as it interacts with the disk and migrates towards the inside of the blue-shifted center of mass curve.

In Fig. 10, we have produced position velocity diagrams for all the runs corresponding to Fig. 7 ($t = 2014.6$). We note that the counter-rotating run has achieved much faster blue-shifted ve-

locities. From Fig. 5, we argue that this is due to the cloud passing much closer to the SMBH. The two inclined runs seem to be less concentrated. The inclined, counter-rotating run shows most of its emission at lower blue-shifted velocities than the non-inclined run. This is due to the disk sweeping the gas out of the line of sight. In the reflected inclined cases, the opposite is true as seen in Fig. 7, because in such configurations the swept gas roughly aligns with the line of sight enhancing the radial velocity component. We know this is purely an effect of the line of sight, because there is no dynamical difference between the inclined, and the inclined and reflected runs. The reflected plots both seem to lie on the outside of the blue-shifted center of mass trajectory, while the unreflected plots are primarily on the inside. In all six cases however, we observe the trend that the counter-rotating runs concentrate at higher blue-shifted velocities than the co-rotating runs. The $1 M_\oplus$ is also primarily on the low velocity side of the center of mass trajectory, indicating it has significantly interacted with the disk. The $300 M_\oplus$ cloud, however, lies precisely along the center of mass trajectory, indicating little or no interaction with the disk.

The differences between the position velocity diagrams are more clearly shown in Fig. 11, where we have plotted contours of fractional mass on the position velocity diagrams for different runs. Again, we see there is clear variation between the counter- and co-rotating clouds in the plane of the disk — the emission from the counter-rotating cloud is more blue-shifted. We also see a clear difference between the most and least massive clouds. The large cloud straddles the center of mass trajectory evenly, while the small cloud contains a significant fraction of low velocity blue-shifted emission. The bottom two plots show how the co- and counter-rotating

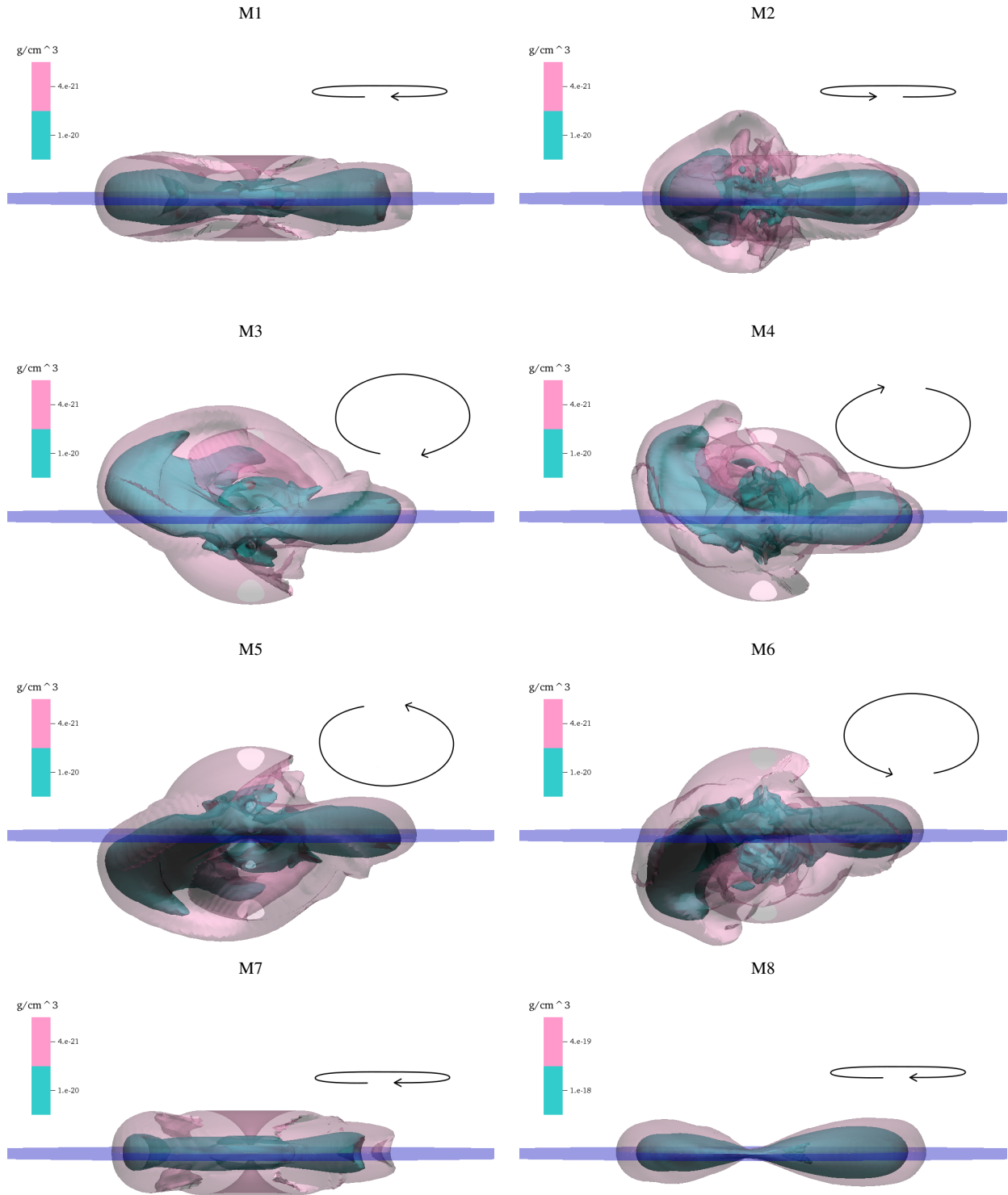


Figure 6. 3D density contour plots at $t = 2014.25$. The line of sight is in the cloud orbital plane from behind the location of pericenter. The blue stripe indicates the orbital plane. The arrows indicate the rotation and orientation of the disk (the arrow heads are protruding). In all cases, the cloud is orbiting from right to left. The horizontal scale is $50,000 R_G$. The contours for model M8 were scaled by two orders of magnitude.

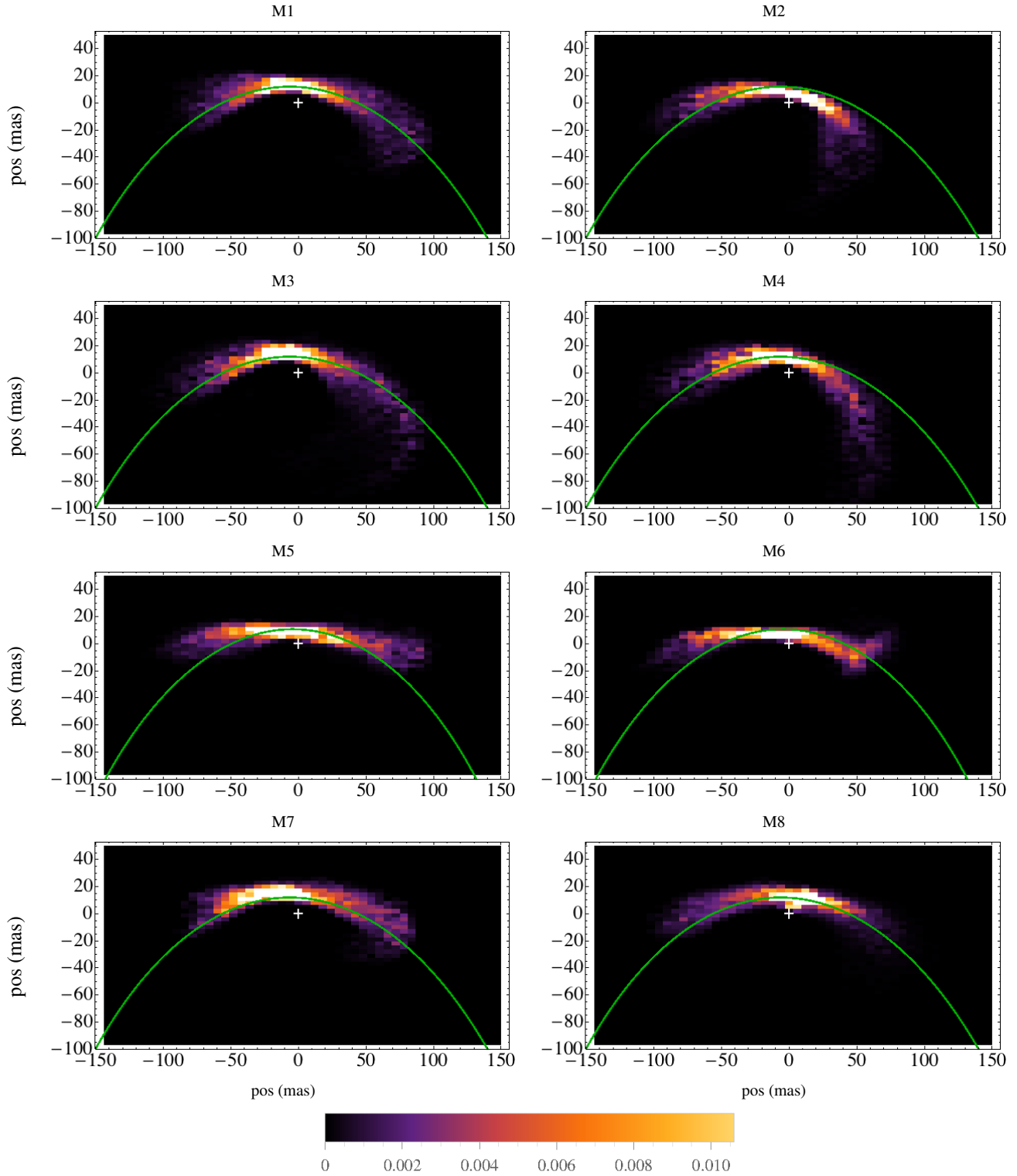


Figure 7. Plots of fractional cloud brightness on the sky at the epoch $t = 2014.6$. The green line shows the trajectory of the center of mass projected on the plane of the sky. The axes are in units of mas, where Sgr A* is at the origin. The colors show the fractional cloud mass.

inclined runs appear to lie on top of each other, and it is only when they are reflected do we notice significant deviation.

6 DISCUSSION

6.1 Detectability

Can the subtle differences between the models we considered be detected? We have discussed the results in terms of the position-

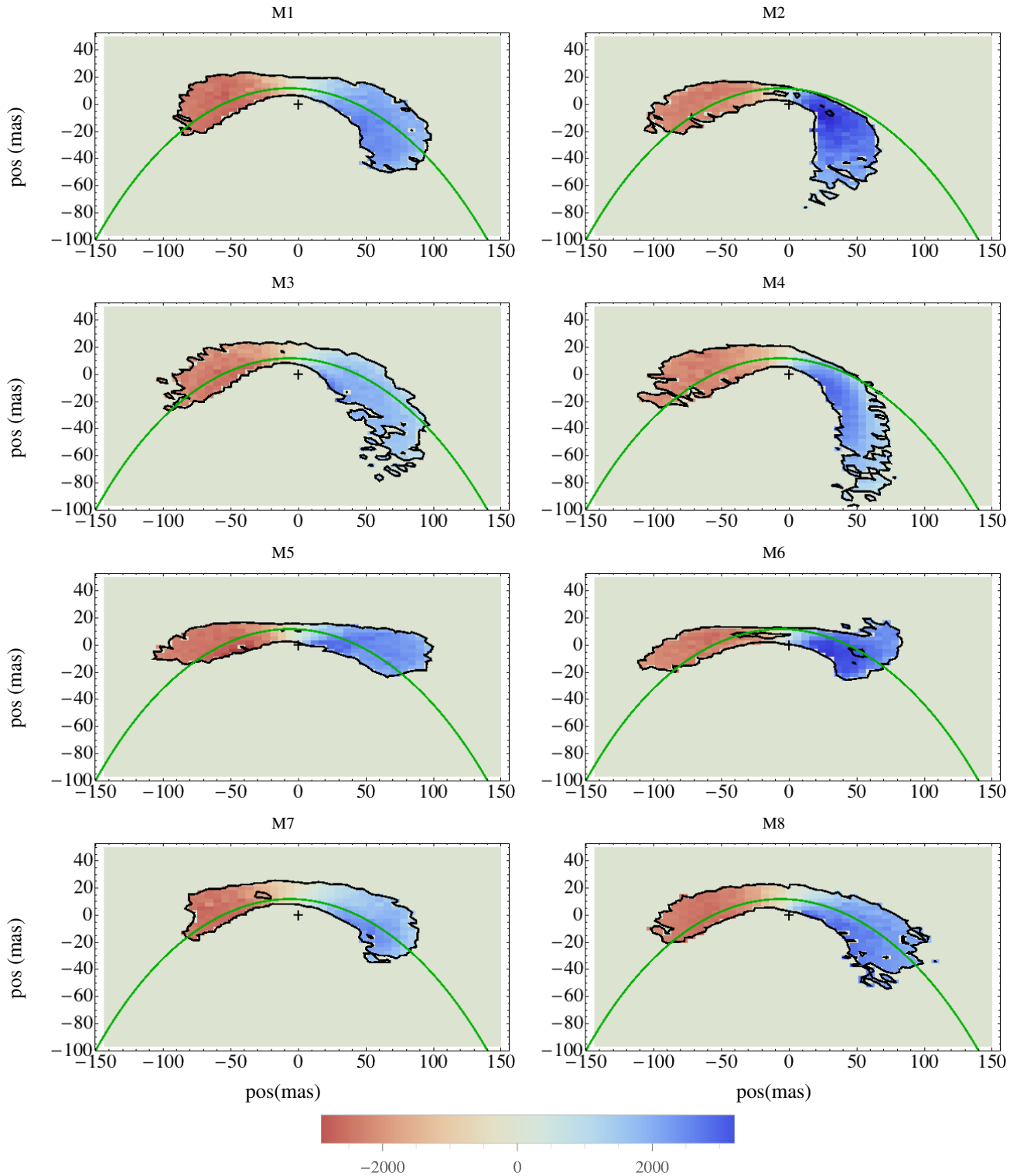


Figure 8. Line of sight velocity plots at $t = 2014.6$. The axes are the same as in Fig. 7. The color scale is in units of km/s. Only points that lie within a fractional mass contour of 10^{-3} (Fig. 7) were plotted. Contours show fractional mass equal 10^{-2} and 10^{-3} .

velocity diagrams and plane of sky images. The former are obtained using state of art adaptive optics and spectrometry. The resolution in velocities (~ 75 km/s) should be enough to distinguish between our counter- and co-rotating models. However, due to degeneracy and uncertainties in cloud and disk parameters, only some con-

straints on them may be put. Plane of sky images and spectroscopy hold more information but the resolution required to resolve the differences between the models ($\lesssim 0.05''$) is beyond the capabilities of current instruments. The GRAVITY project (Gillessen et al. 2010; Kendrew et al. 2012) is expected to have high enough resolution

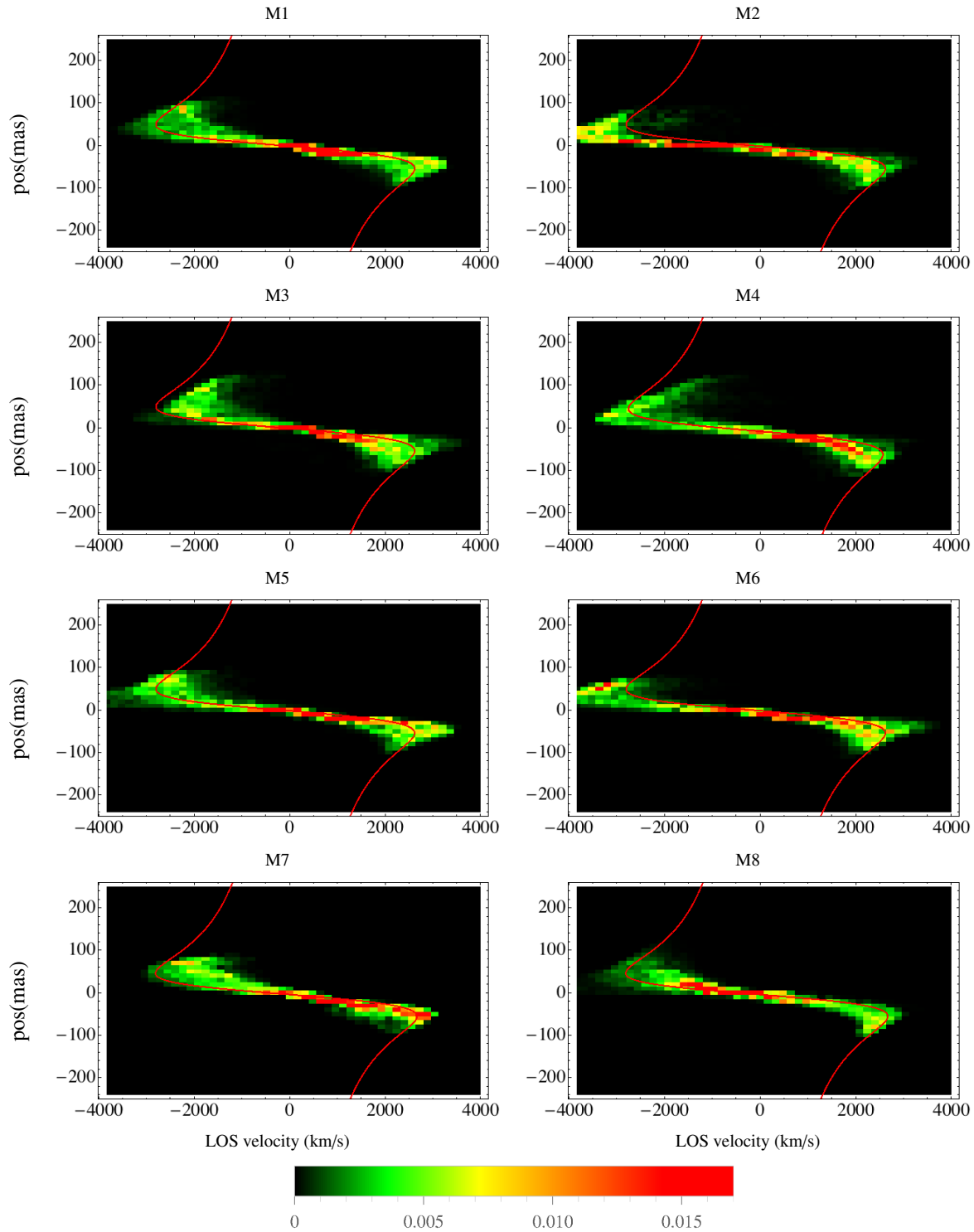


Figure 10. Position-velocity diagrams for models M1-M8 at $t = 2014.6$. The vertical axis indicates distance along the orbit from pericenter in mas. The horizontal axis is line of sight velocity in km/s. The color bar scale is given in fractional cloud brightness. The red line indicates the trajectory of the center of mass.

and may be useful in resolving and interpreting the late stages of the pericenter passage.

Ultimately, what we can say about the parameters of the Sgr A* accretion flow and the G2 cloud is limited by the resolution of future observations and, to an extent, by the degeneracies in our models. We can, however, distinguish between groups of mod-

els. The position velocity diagrams become less degenerate with time. Half a year after pericenter we expect to be able to group the models based on their similarities. M1, M5, and M7 all have over dense regions immediately inside the CM trajectory. M3 and M4, on average, reach lower line of sight velocities so they are concentrated even further inside the CM trajectory. M2 and M6 span

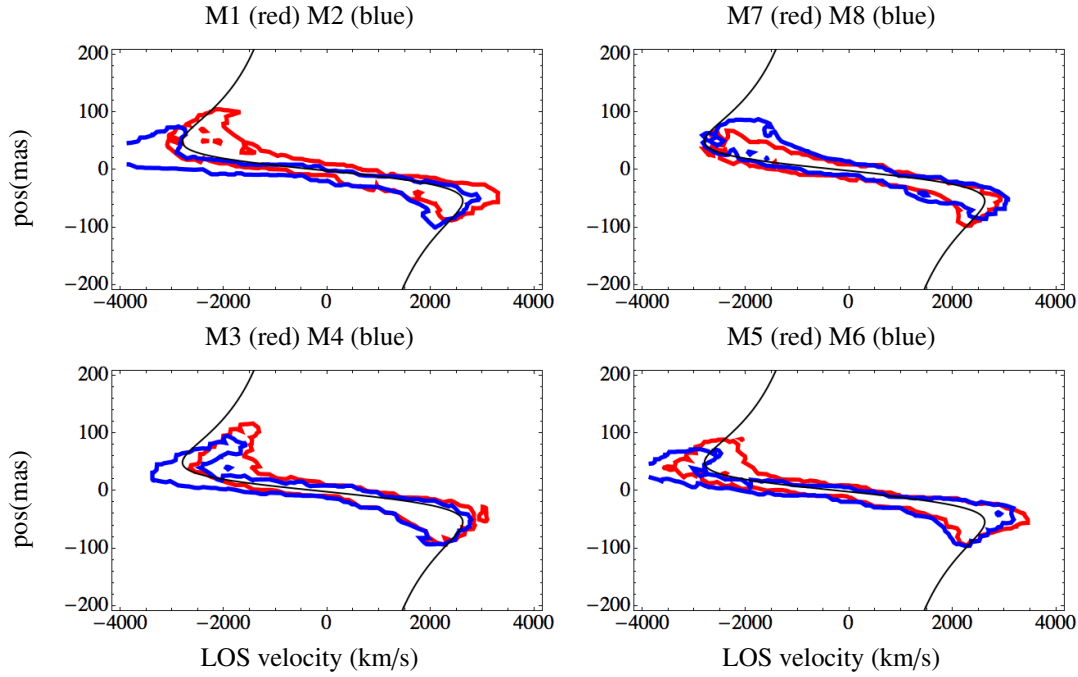


Figure 11. Contours of fractional cloud brightness (0.003) on the position-velocity plots at $t = 2014.6$. Upper left: co-rotating (red) and counter-rotating (blue) models. Upper right: $1 M_{\oplus}$ cloud (red) and $300 M_{\oplus}$ cloud (blue). Lower left: co-rotating and inclined (red) and counter-rotating and inclined (blue). Lower right: Same as lower left but reflected.

a smaller range in positions and reach very large LOS velocities when compared to the other models.

The sky density plots add more information. They would allow us to distinguish, M1 from M5 and M7 due to the degree to which M1 extends below the CM trajectory in comparison. M7 seems to extend above the CM trajectory more so than M5, but not by much. The difference between M3 and M4 is made slightly more clear, because the majority of M4’s emission extends below the CM trajectory. M2 and M6 are very clearly different from each other; M2 has much more emission below the CM trajectory.

The sky LOS velocity plots show slightly slower blue-shifted velocities from M7 and M5, but it is unclear if this would actually be distinguishable.

6.2 Assumptions

Results presented in Section 5 rely on a number of assumptions, as we now explain.

We assumed the G2 cloud is pressure, not momentum, supported. Therefore, our results cannot be applied to the star wind model of the cloud. To model the cloud we took a similar approach to Sądowski et al. (2013) and constructed a cloud of test particles, spherical at $t = 2000.0$, but which was translated onto the numerical grid and evolved together with the accretion flow model since $t = 2012.0$. We chose one particular set of cloud parameters which reasonably reproduces the observed velocities and positions at $t = 2013.4$. However, this set is not unique and other combinations of parameters may lead to similar or better agreement with the observational constraints. We are positive that all of them would result in cloud evolution qualitatively in agreement with the one we studied, especially when taking into account the uncertainty of the mass estimate (Gillessen et al. 2012). One should also keep in mind that the complex structure of the “tail”, which follows the cloud on

the same orbit, suggests that the cloud originated in a complicated process and has not at any point been perfectly spherical.

Another set of caveats is related to the accretion flow model we adopted. Its structure is far from constrained except in the innermost region and close to the Bondi radius. It is tempting, and consistent with numerical simulations, to adopt a power law interpolation between these regions. However, nature may prefer another configuration resulting, for example, in lower than predicted density in the intermediate region. The accretion flow model we use is based on a time- and spatially-averaged numerical solution and therefore does not reproduce the expected turbulent structure. However, its impact on the global picture of the cloud-disk interaction should be negligible. We neglect the magnetic fields

The numerical model we used is also limited. Most importantly, the adopted resolution does not allow to properly resolve Kelvin-Helmholtz instabilities on the cloud surface (Schartmann et al. 2012) or Rayleigh-Taylor instabilities at the head of the cloud (Anninos et al. 2012). Therefore, we were able only to study the interaction of the bulk of the cloud with the disk. The instabilities could produce turbulent structure on the cloud surface which may enhance the interactions. The differences between different models discussed in Section 5 could be, in these terms, considered conservative. Another limitation of our numerical approach is the necessity of stabilizing the atmosphere using the tracer field. Such an approach may lead to under resolving the leading bow-shock region. However, by performing simulations with different values of the critical tracer value (Models P4 and P5) we have shown that it has no impact on the qualitative picture.

In this work we assumed that the luminosity is proportional to the total density, i.e., we did not distinguish the cloud density from the density of the original accretion disk. The cloud gas is few orders of magnitude more dense, so this assumption may have little effect. However, we also did assume that the luminosity depends only on the density. In reality, it may be sensitive to other param-

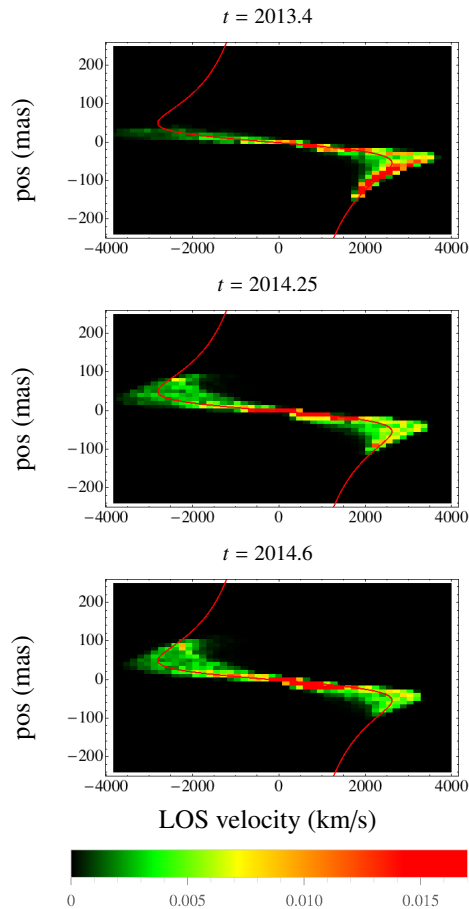


Figure 9. Position-velocity plots for the co-rotating disk corresponding to epochs $t = 2013.4, 2014.25, 2014.6$. The vertical axis indicates distance along the orbit from pericenter in mas. The horizontal axis is line of sight velocity in km/s. The colors indicate the fractional cloud mass.

ters, e.g., ionization fraction. To better model the observed properties of the cloud one should perform more sophisticated radiation-transfer simulations, similar to the ones presented in Shcherbakov (2013).

7 SUMMARY

In this work we have studied the effect of the rotating gas in the vicinity of Sgr A* on the appearance of G2 after pericenter. We have assumed the cloud is pressure supported and adopted the self-similar model of accretion flow by Sądowski et al. (2013b), i.e., we assumed the density profile has a slope r^{-1} between the SMBH and the Bondi radius. We have shown that the momentum of the innermost parts of the accretion flow is sufficient to significantly affect the cloud evolution. Therefore, the cloud properties after it crosses the pericenter will also depend on the gas properties of the accretion flow.

We have performed a set of 14 hydrodynamical, three dimensional simulations. In models M1-M6 we studied the importance of the orientation of the cloud orbit with respect to rotation of the disk. In models M7 and M8 we considered clouds of a lower and higher masses. The parameter study we performed (models P1-P6) has shown our results are to a good accuracy parameter independent.

In all the models we evolved the cloud-disk system until the epoch $t=2014.6$ and studied properties of the cloud by calculating position-velocity diagrams and plane of sky images. Various models led to visibly different signatures. However, the differences are at the edge of detectability for position-velocity diagrams and out of current range for the sky-plane images. The latter may change if Gravity (Gillessen et al. 2010; Kendrew et al. 2012) becomes operational early enough.

The results presented in this work will help distinguish between the pressure- and momentum-supported models of the cloud. It is also likely they will give constraints on the nature of the Sgr A* accretion flow and the G2 cloud itself.

8 ACKNOWLEDGEMENTS

A.S. is supported in part by NASA grant NNX11AE16G. L.S. is supported by NASA through Einstein Postdoctoral Fellowship grant number PF1-120090 awarded by the Chandra X-ray Center, which is operated by the Smithsonian Astrophysical Observatory for NASA under contract NAS8-03060. We thank Ramesh Narayan and Maciek Wielgus for helpful discussions.

REFERENCES

- Abramowicz, M., Jaroszynski, M., & Sikora, M. 1978, *Astronomy & Astrophysics*, 63, 221
- Anninos, P., Fragile, P. C., Wilson, J., & Murray, S. D. 2012, *Astrophysical Journal*, 759, 132
- Baganoff, F. K., Maeda, Y., Morris, M., et al. 2003, *Astrophysical Journal*, 591, 891
- Ballone, A., Schartmann, M., Burkert, A., et al. 2013, arXiv:1305.7238
- Broderick, A. E., Fish, V. L., Doeleman, S. S., & Loeb, A. 2011, *Astrophysical Journal*, 735, 110
- Burkert, A., Schartmann, M., Alig, C., Gillessen, S., Genzel, R., Fritz, T. K., & Eisenhauer, F. 2012, *Astrophysical Journal*, 750, 58
- Dexter, J., Agol, E., Fragile, P. C., & McKinney, J. C. 2010, *Astrophysical Journal*, 717, 1092
- Dibi, S., Drappeau, S., Fragile, P. C., Markoff, S., & Dexter, J. 2012, *Monthly Notices of the Royal Astronomical Society*, 426, 1928
- Gammie, C. F., McKinney, J. C., & Tóth, G. 2003, *Astrophysical Journal*, 589, 444
- Gillessen, S., Eisenhauer, F., Perrin, G., et al. 2010, *Proceedings of the International Society for Optical Engineering*, 7734,
- Gillessen, S., Genzel, R., Fritz, T. K., et al. 2012a, *Nature*, 481, 51
- Gillessen, S., Genzel, R., Fritz, T. K., et al. 2013, *Astrophysical Journal*, 763, 78
- Gillessen, S., Genzel, R., Fritz, T. K., Eisenhauer, F., Pfuhl, O., Ott, T., Schartmann, M., Ballone, A., & Burkert, A. 2013, arXiv:1306.1374
- Guillochon, J., Loeb, A., MacLeod, M., & Ramirez-Ruiz, E. 2014, arXiv:1401.2990
- Kendrew, S., Hippler, S., Brandner, W., et al. 2012, *Proceedings of the International Society for Optical Engineering*, 8446,
- Marrone, D. P., Moran, J. M., Zhao, J.-H., & Rao, R. 2007, *Astrophysical Journal Letters*, 654, L57
- Mościbrodzka, M., Gammie, C. F., Dolence, J. C., Shiokawa, H., & Leung, P. K. 2009, *Astrophysical Journal*, 706, 497
- Narayan, R., & Yi, I. 1994, *Astrophysical Journal Letters*, 428, L13
- Narayan, R., Sądowski, A., Penna, R. F., & Kulkarni, A. K. 2012b, *MNRAS*, accepted
- Osterbrock, D. E., & Ferland, G. J. 2006, *Astrophysics of gaseous nebulae and active galactic nuclei*, 2nd. ed. by D.E. Osterbrock and G.J. Ferland. Sausalito, CA: University Science Books, 2006,
- Phifer, K., Do, T., Meyer, L., Ghez, A. M., Witzel, G., Yelda, S., Boehle,

- A., Lu, J. R., Morris, M. R., Becklin, E. E., & Matthews, K. 2013, arXiv:1304.5280
- Saitoh, T. R., Makino, J., Asaki, Y., et al. 2012, arXiv:1212.0349
- Shcherbakov, R. 2013, submitted to ApJ
- Sądowski, A., Narayan, R., Tchekhovskoy, A., & Zhu, Y. 2013a, Monthly Notices of the Royal Astronomical Society, 429, 3533
- Sądowski, A., Sironi, L., Abarca, D., et al. 2013b, arXiv:1301.3906
- Sądowski, A., Narayan, R., Sironi, L., Ozel, F. 2013, Monthly Notices of the Royal Astronomical Society, 433, 2165
- Schartmann, M., Burkert, A., Alig, C., et al. 2012, Astrophysical Journal, 755, 155
- Shcherbakov, R. V., Penna, R. F., & McKinney, J. C. 2012, Astrophysical Journal, 755, 133
- Wang, Q. D., et al. 2013, astro-ph/1307.5845
- Yuan, F., Quataert, E., & Narayan, R. 2003, Astrophysical Journal, 598, 301
- Yuan, F., Wu, M., & Bu, D. 2012, Astrophysical Journal, 761, 129